Fluid Transport in Partially Shielded Electrowetting on Dielectric Digital Microfluidic Devices

Andrew C. Madison, *Member, IEEE*, Matthew W. Royal, and Richard B. Fair, *Life Fellow, IEEE*

Abstract—Theoretical and experimental approaches verifying the fluidic operation of a partially shielded digital microfluidics device are presented in this paper. This paper is motivated by recent demand from the synthetic biology community for electrowetting on dielectric (EWD) enabled in-droplet electroporation, but is generalizable to a range of EWD applications that require shielding structures to be patterned on the EWD. An electrode patterned in an additional metal layer on the insulator that supports EWD actuation reduces the effective strength of the EW force due to dielectric shielding at the droplet contact line. A numerical model was developed to predict the impact of the partially shielding electrode on threshold voltage, EW force, fluid velocity, and droplet transport time. Compared with a batch of devices lacking the extra electrode, the presence of the added metal layer resulted in a 29% increase in threshold voltage, an 82% increase in transport time, and a 44% decrease in average transport velocity. Each trend agrees with the simulation results obtained from the fluid transport model. These results support the development of design rules for microfluidic devices that require partially shielding metal layers to integrate with EWD device architectures.   **[2016-0034]**

Index Terms—Fluidics, transport, model, mechanics, finite element model, electrowetting on dielectric, electroporation, gene transfer, electrotransfer, device, digital microfluidics.

I. Introduction

ELECTROWETTING on dielectric (EWD) devices are microelectromechanical systems (MEMS) that utilize precisely applied electric potentials to generate an electrowetting force that counteracts surface tension forces acting at a fluid interface and ultimately, drives fluid motion at reduced geometric scales. Since its discovery in 1875 [1], the electrowetting effect has been leveraged in a diverse array of MEMS applications including microfluidic actuation in laboratory on chip (LoC) platforms [2]–[8], dynamic microlenses [9], electronic displays [10], [11], and energy harvesting devices [12]. Alongside these experimental breakthroughs, the theoretical underpinnings of EWD-based MEMS has matured to cover a near complete understanding of the fluid dynamics that govern fluid transport in the systems.

Theoretical approaches to understanding the phenomenological nuances of EWD drive the optimization of EWD-based MEMS devices. Although the general dynamics of fluid transport in EWD platforms are well-understood, modeling performance issues associated with contact line pinning, contact angle saturation and hysteresis still requires considerable approximation [13]–[20]. Nevertheless, analytical and numerical approaches toward modeling EWD devices produce simulations that agree quite well with experimental results [14], [15], [17].

As EWD device models have matured, experimentalists have advanced the scope of the technology by integrating a wide assortment of components with the EWD electrode architecture. Multilayer and coplanar geometries are reported for the integration of resistive heaters [21]–[24] and temperature sensors [24]; windows for on-chip optical interrogation [22], [25], [26]; microelectrodes for impedance spectroscopy [27] and particle separation based on electro- and magnetophoresis [28], [29]; as well as bio-functionalized electrode regions for cell culture [30], field effect transistor biosensors [31], and surface plasmon resonance-based DNA detection [32], [33]. Although these additional elements expand the capability of their respective EWD devices, they are not free of cost. The integration of new components into the EWD device framework often reduces the electrode area available for droplet actuation, which reduces the resultant magnitude of an applied electrowetting force and ultimately, compromises the ability of the device to support fluid transport [26]. Thus, understanding the impact that integrated components have on fluid transport in an EWD platform is important for device optimization and further expansion of the EWD toolkit.

Our work applies established theoretical models of EWD transport phenomena and basic droplet transport experiments to understand the impact of a multilayer component integrated into an otherwise typical EWD platform. In this paper, we analyze fluid transport in the presence and absence of a scalable electroporation (EP) device integrated as an additional metal trace deposited on the EW dielectric. Ideally, EP of cells in suspension is carried out through the application of a spatially-uniform electric field pulse. However, we found that integration of EP and EWD electrodes requires (1) the EP electrode layer to be in close electric contact with the droplet to ensure exposure to the EP field; and (2) the EP electrode to be patterned with a geometry that exposes the underlying EWD electrode to the droplet interface to ensure application of the electrowetting force. In meeting these constraints, the marriage of EP and EWD capabilities enables the bulk transfer
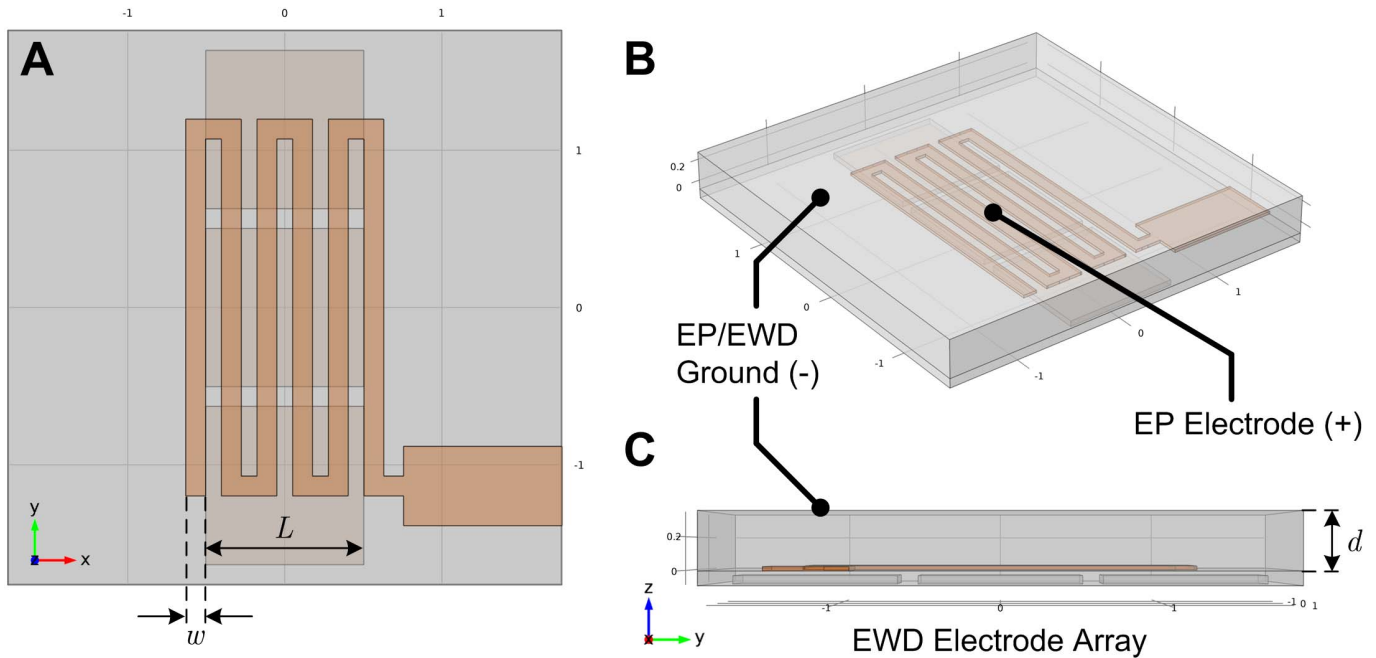
Fig. 1. EWD/EP Integration. (A) Top view (*xy*-plane) of the integrated EP/EWD device. EWD electrode length and EP electrode width are labeled L and w, respectively. (B) Isometric projection of the EP/EWD device showing the EP electrode and the planar EWD counter electrode as the common EP/EWD ground. (C) Side view (*yz*-plane) of the integrated EP/EWD device. The channel height, set by the gasket, is labeled d.

of exogenous DNA into microbial cell populations confined within an EWD-actuated droplet [34], but is expected to significantly reduce the efficacy of the applied EW force due to dielectric shielding of the EWD electrode by the EP electrode. Hence, in our case understanding the impact that multilayer device integration has on droplet transport is critical to implementing high-efficiency gene transfer in an EWD-based LoC.

We report theoretical and experimental approaches used to model and verify an EWD-based digital microfluidics device that leverages a partially shielding metal layer on the EW dielectric as an EP electrode. We applied the numerical model reported by Walker and Shapiro [17] to a hybrid EP/EWD device geometry to predict the effects that the EP layer has on three fluid transport parameters: threshold voltage, EW force, fluid velocity, and droplet transport time. Subsequently, we evaluated the model's predictions by measuring the same three fluid transport parameters for 8 devices fabricated in-house. Performance with respect to bacterial transformation for the EP/EWD device is reported elsewhere [34].

Walker and Shapiro utilized the level-set, finite element method (FEM) model in conjunction with the standard Navier-Stokes formulation and approximate effects of contact angle hysteresis to successfully predict a droplet's liquid-gas interface during EWD actuation in a two dimensional computational domain [17]. Our approach advances their simulation technique by applying a nonhomogeneous scalar field that introduces the electric shielding effect that the metallic EP electrode imparts to eclipsed regions on the EWD electrode. Thus, our numerical modeling approach incorporates dynamics associated with viscid fluid flow, contact angle hysteresis, and EWD electrode inhomogeneity to predict droplet transport in a hybrid EP/EWD device.

Geometric parameters of the proposed EP/EWD device are outlined in Section II. The mathematical model used in the parametric simulation of the device is outlined in Section III and, theoretical results from the numerical model are presented in Section IV. The experimental method used for device characterization is discussed in Section V, and a comparison of experimental and theoretical results is presented in Section VI.

II. DEVICE GEOMETRY

The integrated device consists of a metal layer patterned on top of the EW dielectric and a counter electrode on the EWD top plate. This configuration enables a high electric field pulse to be applied to cells confined within a droplet held in place by the underlying EWD electrode. As shown in Figure 1 (A), the EP/EWD device is oriented such that its long edges run parallel to the EWD electrode array, in the $\hat{y}$-direction. This orientation ensures exposure of the droplet contact line to the underlying EWD electrode. An array of EWD electrodes of length, L, appear beneath the EP electrode and EW dielectric. The meandering EP electrode makes six passes over the center EWD electrode, four of which eclipse EWD electrode. The width of the EP wire is noted as, w, and in Figure 1 is modeled with a width, $w = L/8$. In the simulations that follow, the EP wire width is parameterized to assess its impact on electric fluidic transport.

Figure 1 (B) shows an isometric projection of the EP/EWD device layout. The EP electrode is labeled alongside the common EP/EWD ground electrode. Since each device layer is drawn to scale the EW dielectric, which has thickness t, is too thin to be seen, but is partially opaque in color and shades the underlying EWD electrodes. Thus, the EP/EWD design relies upon the EP electrode to be patterned on top of the EW dielectric. Figure 1 (C) shows the side view (*yz*-plane) of the

EP/EWD device. In this view, the EW dielectric can be seen separating the EP and EWD electrodes. The channel height, set by the gasket, is labeled d.

As shown in Figure 1 (B,C), the top plate is a common counter electrode for both the EP and EWD circuits. For clarity, the top plate is depicted as a slice in the xy-plane where $z = d = L/3$. In the implementation of the device, the top plate has a finite thickness. This thickness is inconsequential to the electric field profile within the droplet and accordingly is omitted to make the EP/EWD geometry more obvious. The important feature to note is the planar electrode on the top plate, which provides the electrical ground for both EP and EWD electrodes.

III. THEORETICAL FRAMEWORK

To address the impact of EP/EWD integration on droplet transport, an FEM model of EWD fluid dynamics was developed using the Laminar Two-Phase Flow, Level Set interface in COMSOL MULTIPHYSICS®. The purpose of this analysis is to investigate and quantify the effects that the geometry of the EP electrode has on EWD fluid transport. Of particular interest are the threshold voltage, electrowetting force, fluid velocity, and droplet transport time in the integrated EP/EWD device compared to baseline EWD performance.

Rather than solving for the electrical field around the droplet and the resultant electrowetting force present during actuation, the present model uses the Young-Lippmann approximation to reduce the contact angle of the droplet in areas not shielded with the EP electrodes. Under the assumption that the devices operate well under the threshold of contact angle saturation, the reduction in contact angle reduces the Laplace pressure at the advancing edge of the droplet, introducing a net force equal to the net electrowetting force on the droplet [35].

A. Governing Equations

The level set interface uses the incompressible formulation of the Navier-Stokes Equations (1–2) along with the level set function from Eq. 3 to track the interface of two immiscible fluids [36]. We present the governing equations of the fluid transport model below:

$$\rho \frac{\partial \mathbf{u}}{\partial t} + \rho (\mathbf{u} \cdot \nabla) \mathbf{u} = \nabla \cdot \left[p\mathbf{I} + \mu \left(\nabla \mathbf{u} + \nabla \mathbf{u}^\mathsf{T} \right) \right] + \mathbf{f} \quad (1)$$

$$\nabla \cdot \mathbf{u} = 0 \quad (2)$$

$$\frac{\partial \phi}{\partial t} + \mathbf{u} \cdot \nabla \phi = \gamma_{LV} \nabla \cdot \left[\varepsilon \nabla \phi - \phi (1 - \phi) \, \hat{\mathbf{n}}_i \right] \quad (3)$$

$$\rho = \rho_2 + (\rho_1 - \rho_2) \, \phi \quad (4)$$

$$\mu = \mu_2 + (\mu_1 - \mu_2) \, \phi \quad (5)$$

$$\phi = \begin{cases} 1 : & \text{for fluid 1} \\ 0 : & \text{for fluid 2} \end{cases} \quad (6)$$

where $\mathbf{u}$ is the fluid velocity, $\mathbf{I}$ is the identity matrix, and γ_{LV} is the interfacial surface tension between the two fluids. In this formulation, the level set variable, ϕ, is a scalar field value that is equal to 1 for locations in the domain that correspond to fluid 1 (cells) and 0 for fluid 2 (silicone oil). The level set variable facilitates the mapping of scalar and vector quantities associated with the fluid interface, such as the density (ρ) and

viscosity (μ) per Eq. 4–5. In this context the surface normal of the fluid interface is defined as $\hat{\mathbf{n}}_i = \frac{\nabla \phi}{\|\nabla \phi\|}$, where $\nabla \phi$ is non-zero over the interface thickness, ε, and zero elsewhere. This coupled system allows for applied forces, pressures, and velocities to influence the spatio-temporal dynamics of the fluid interface.

B. Forcing Equation

In our model, the surface tension and electrowetting forces, which respectively act on the fluid interface and contact line, are included in the Navier-Stokes forcing term, $\mathbf{f}$. As previously described, the surface tension force, $\mathbf{f}_{ST}$, may be attributed to the principle curvatures of the fluid interface, κ_{xy} and κ_z, while the electrowetting force, $\mathbf{f}_{EW}$, may be introduced as a voltage-dependent perturbation of the z-curvature, κ_z, of the droplet interface [14], [18], [36], [37]. While the xy-curvature is simply written as the negated divergence of the $\hat{x}$ and $\hat{y}$ components of the interface normal (Eq. 7), the voltage-dependent z-curvature may be approximated by Eq. 8 provided the height of the droplet is much smaller than its diameter [17], [18].

$$\kappa_{xy} = -\nabla \cdot \hat{\mathbf{n}}_i \quad (7)$$

$$\kappa_z (V) = -\frac{1}{d} \left[\cos \theta_Y + \cos \theta_{EW} (V (\mathbf{x})) \right] \quad (8)$$

where θ_Y is the zero-voltage contact angle, θ_{EW} is the wetting angle of the droplet under actuation, $V (\mathbf{x})$ is the spatially-dependent electric potential, and $\mathbf{x} = (x, y) \in \mathbb{R}^2 : -2L \le x \le 2L, -2L \le y \le 2L$. This simplification collapses the z dimension of the problem, allowing the simulation to occur in $\mathbb{R}^2$ rather than $\mathbb{R}^3$, which offers tremendous savings in computational cost and allows numerical solutions to be obtained on a desktop workstation within reasonable timeframes.

Taking advantage of these estimates along with the Young-Lippmann equation and a scaling factor, κ_{Hys}, used by Walker and Shapiro to account for contact angle hysteresis, the Navier-Stokes forcing term for droplet motion in the EWD device model is written in the following way [14], [17], [38], [39]:

$$\mathbf{f} = \mathbf{f}_{ST} + \mathbf{f}_{EW} \quad (9)$$

$$= -\frac{\kappa_{Hys} \gamma_{LV}}{d} \left(\kappa_{xy} + \frac{L}{d} \kappa_z (V (\mathbf{x})) \right) \hat{\mathbf{n}}_i \quad (10)$$

$$= -\frac{\kappa_{Hys} \gamma_{LV}}{d} \left(\kappa_{xy} + \frac{L}{d^2} \left[2 \cos \theta_Y + \frac{\varepsilon_r \varepsilon_0}{2t \gamma_{LV}} V (\mathbf{x})^2 \right] \right) \hat{\mathbf{n}}_i \quad (11)$$

Note that the electrowetting number, $\eta = \frac{\varepsilon_r \varepsilon_0}{2t \gamma_{LV}} V^2$, appears in the formulation of the forcing term. The term, κ_{Hys} scales the forcing term in Eq. 1 by a positive value less than or equal to 1, and is estimated as a function of the zero-voltage wetting angle, θ_Y, the angle of hysteresis, α, and the voltage-dependent EW contact angle, θ_{EW}, in the following form.

$$\kappa_{Hys} = \frac{2 \cos (\theta_Y - \alpha) - \cos (\theta_Y + \alpha) - \cos (\theta_{EW} + \alpha)}{\cos \theta_Y - \cos \theta_{EW}} \quad (12)$$

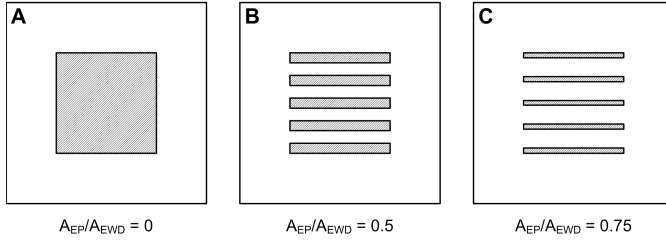$$0 \le \kappa_{Hys} \le 1 \quad (13)$$

Fig. 2.   EP/EWD Electrode Shielding. (A) Baseline EWD case where $A_{\text{EP}}/A_{\text{EW}} = 0$ and the EP electrode is absent. (B) $A_{\text{EP}}/A_{\text{EW}} = 0.5$; and (C) $A_{\text{EP}}/A_{\text{EW}} = 0.75$. In each plot, the contours show where θ_{EW} was augmented to simulate segments of the EWD electrode that are unshielded by the EP electrode. Shaded areas indicate unshielded regions of the EWD electrode.

Droplet motion was driven by applying a voltage, which reduced the electrowetting angle in unshielded regions of the EWD electrode in the xy-plane. For each simulation, θ_{EW} was defined as a scalar field variable that corresponds to the location of unshielded segments of the EWD electrode. To simulate the activation of the EWD electrode, a step function was used to quickly ramp the applied voltage, V; this caused θ_{EW} to shift from the zero-voltage value, θ_{Y} to the EW voltage-dependent value, θ_{EW}, per the Young-Lippmann equation. This stimulus reduces the z-curvature, κ_z, per Eq. 8, and results in a net force on the fluid interface that causes the droplet to move toward the energized electrode.

Figure 2 shows the scalar field data used to model EWD electrodes that would be shielded by an overlying EP electrode. The shaded areas in the figure indicate regions of the EWD electrode that are not shielded by the EP electrode. The model asserts that unshielded regions of the EWD electrode include grid points where the local contact angle transitions from θ_{Y} to θ_{EW}, if the droplet interface happens to coincide with these regions. Figure 2 (A) depicts the baseline case where the EP wire is absent and the fractional area of EP to EWD electrode coverage equals zero. Thus, baseline EWD operation is recovered when $A_{\text{EP}}/A_{\text{EW}} = 0$ because there is no EP electrode present to shield the EWD electrode. In contrast, Figures 2 (B) and (C) show cases where the EP electrode width is non-zero, and $A_{\text{EP}}/A_{\text{EW}} = 0.5$ and $A_{\text{EP}}/A_{\text{EW}} = 0.75$, respectively. Since the net force on the droplet is proportional to the volume integral of the surface tension force, which is modulated at the contact line by θ_{EW} and enveloped by $A_{\text{EP}}/A_{\text{EW}}$, it follows that as the fractional area of electrode coverage, $A_{\text{EP}}/A_{\text{EW}}$, increases the magnitude of the net body force should decrease to zero.

C. Boundary Conditions

The proposed EP/EWD device simulation includes two types of boundaries that include two stationary walls, where the EWD channel wall is presumed to be, as well as two open boundaries, which are treated as fluid inlets/outlets in that fluid is free to move across the boundary in either direction. The stationary walls were parallel to the direction of droplet transport while the open boundaries were positioned perpendicular to the direction of droplet motion. The boundary

TABLE I
PHYSICAL PARAMETERS

Parameter	Symbol	Value	Units
Density* Fluid 1, cells	ρ_1	1.05	g·cm^{-3}
Density* Fluid 2, silicone oil	ρ_2	0.89	g·cm^{-3}
Viscosity†,‡ Fluid 1, cells	μ_1	0.001	Pa·s
Viscosity†,‡ Fluid 2, silicone oil	μ_2	0.002	Pa·s
Surface Tension‡	γ_{LV}	56	mN·m^{-1}
Interface Thickness*	ϵ	2	μm
Electrode Length*	L	700	μm
Channel Height *	d	230	μm
Dielectric Thickness*	t	2	μm
Dielectric Constant$^{\bullet}$	ε_{r}	3	
Young's Angle‡	θ_{Y}	160	$^{\circ}$
Hysteresis Angle‡	α	2	$^{\circ}$
Reference Pressure*	p_0	0	Pa

∗ Measured parameter.
† Denotes dynamic viscosity.
‡ Parameter estimated from micrograph, *e.g.* pendant drop method.
⋆ Computational or geometric parameter.
• Reported parameter, [40].

conditions for the fluid transport analysis are as follows:

$$\mathbf{u} = 0 \text{ at } y = \pm 2L \qquad (14)$$

$$p = p_0; \quad \left[\mu \left(\nabla \mathbf{u} + (\nabla \mathbf{u})^{\mathsf{T}} \right) \right] \cdot \mathbf{\Theta} = 0 \text{ at } x = \pm 2L \quad (15)$$

D. Initial Conditions

Initial conditions were chosen such that the fluid velocity is zero everywhere at $t = 0$, and the pressure inside the droplet reflects the Young-Laplace condition of a droplet of radius, R_{d}, in an immiscible fluid since the Eötvös (Bond) number is much less than unity, $\frac{\Delta \rho g L^2}{\gamma_{\text{LV}}} \simeq 0.01372 \ll 1$.

$$\mathbf{u}\,(x, y; t = 0) = 0 \qquad (16)$$

$$p = p_0 + \frac{2\gamma_{\text{LV}}}{R_{\text{d}}}\phi \qquad (17)$$

A Delaunay triangular mesh ranging in element spacing from 1 μm – 50 μm was applied to the planar geometry. A convergence study revealed that this mesh density provided acceptable solution accuracy while minimizing computation time. Over 25,000 grid points were included within the $4L \times 4L$ sized domain. To analyze the fluidic impact of the EP/EWD device geometry, the fluid phase, pressure, and velocity fields were computed for a range of wire widths ranging from 0 to $L/4$. Simulations required 3–8 hrs of computation time and were completed on a desktop computer equipped with the 3.2 GHz Intel quad-core Xenon processors and 16 GB of RAM. Lastly, a list of the physical parameters for the geometry of the EP/EWD device as well as fluid parameters for a ~3.3 OD$_{600}$ suspension of *E. coli* cells in 0.05% Tween-20 and 2 cSt silicone oil is given in Table I.

IV. SIMULATION RESULTS

Solutions of the theoretical model described in the preceding section were computed for a range of EP electrode geometries parameterized by, w, the EP electrode width including the
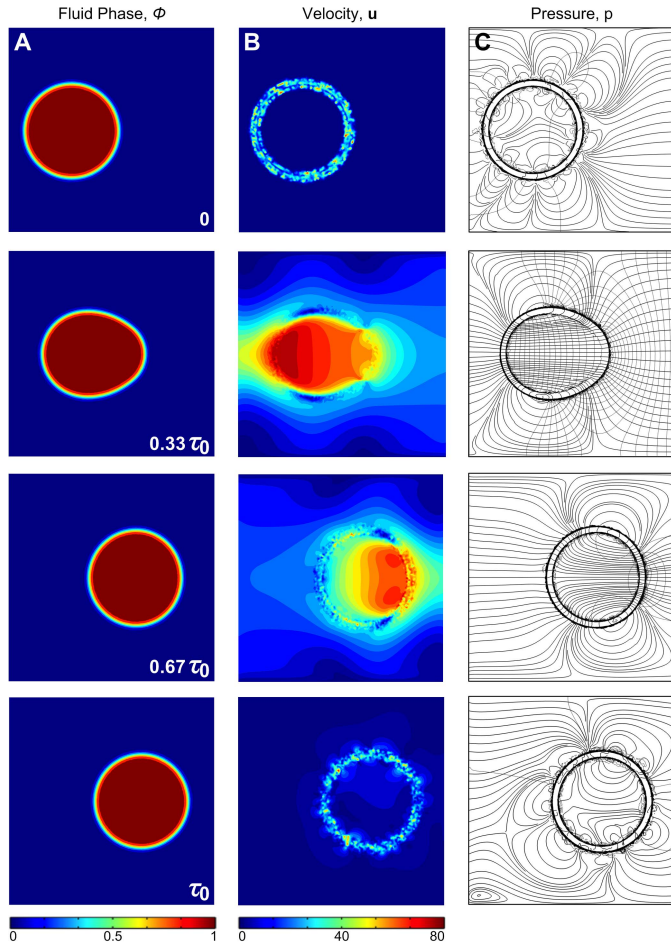
Fig. 3. Baseline EWD fluid transport analysis results for an unobstructed EWD electrode in which $A_{EP}/A_{EW} = 0$; ($w = 0$). (A) Fluid phase, ϕ; (B) velocity magnitude, $\|\mathbf{u}\|$, where units in the scale bar below are in mm·s^{-1}; (C) contours of the pressure field, p.

baseline case in which $w = 0$ and the EP electrode is absent. Widths of the EP wire included $w = 0$, $\frac{L}{16}$, $\frac{L}{8}$, $\frac{3L}{16}$, $\frac{7L}{32}$, and $\frac{L}{4}$. The baseline case is shown in Figure 3, which depicts the (A) fluid phase, ϕ, (B) velocity magnitude, $\|\mathbf{u}\|$, and (C) contours of the fluid pressure, p with an overlay of velocity streamlines computed for typical EWD actuation. The simulation time is noted in terms of the baseline transport time, τ_0, in the lower right hand corner of column (A). Taken together, the plots reveal the dynamics of unobstructed EWD actuation. The phase field, in column (A), shows the droplet in red and the silicone oil filler fluid in blue. Once the EWD electrode is energized, the interface deforms under the unbalanced stress of the electrowetting force. This results in a pressure differential that moves the droplet to the right, toward the activated EWD electrode.

Column (B) of Figure 3 depicts droplet transport in a more detailed view of the EWD transport dynamic. At $t = 0$, the only fluid velocity observable is due to small pressure gradients in the curvature of the droplet interface. However, once the neighboring EWD electrode is energized, the reduction in z-curvature due to the change contact angle change induces fluid motion throughout the microfluidic channel.

The advancing edge of the droplet creeps over the EWD electrode as its trailing edge accelerates to nearly 80 mm/s. Per the no-slip boundary conditions applied to the top and bottom of the computational domain, the fluid velocity decays away from the droplet, eventually reaching zero at the channel walls, where $y = \pm 2L$.

At the onset of droplet motion, the velocity magnitude is greater at the leading edge of the droplet and the droplet deforms, elongating as it moves to the neighboring energized electrode. As the droplet stretches, surface tension in the droplet interface causes the trailing edge to spring forward as the droplet centroid transitions between electrodes. This snapping motion causes a transient increase in the velocity magnitude in the rear of the droplet, which is shown in the second panel of Figure 3 (B). As the interface curvature stabilizes, the droplet regains its circular shape, and again the velocity magnitude in the leading edge of the droplet exceeds that of its trailing edge, as shown in the third panel of Figure 3 (B), before coming to rest on the energized electrode.

Column (C) of Figure 3 shows pressure contours and velocity streamlines of the unobstructed droplet transport process. As the EWD electrode is turned on, pressure contours immediately form around the advancing droplet edge. The pressure gradient, ∇p, as indicated by the density of contour lines generates motion in the fluid that is visualized by streamlines that follow the direction of the pressure gradient and therefore, perpendicular to the contours of pressure. Thus, the overlay of pressure contours and streamlines resembles a grid that deforms around the advancing droplet. The streamlines also indicate two circulation currents that appear as concentric arcs, which are seen on the top and bottom sides of the droplet during transport when $t = 0.33\tau_0$ and $t = 0.67\tau_0$. Lastly, the thickness of the fluid interface, ε, is clearly shown in Column (C).

To gain insight on the fluidic impact of the EP electrode design, the droplet transport analysis was repeated for a range of values of $A_{EP}/A_{EW} = \frac{4w}{L}$. We begin with a qualitative comparison of cases in which the EP electrode is present and absent and later, quantify the effect of the presence of the EP electrode for a range of EP electrode widths. Figure 4 shows the results from the droplet transport analysis conducted with an EP electrode width of $w = \frac{3L}{16}$ or $A_{EP}/A_{EW} = 0.75$. This corresponds to the shielding case depicted in Figure 2 (C). The plots in Figures 3 and 4 are drawn with the same color and size scales to facilitate direct comparison.

As before, the fluid phase, velocity, and pressure are respectively visualized in surface, contour, and streamline mappings. Simulation time is indicated in terms of the baseline EWD transport time, τ_0, in the lower right corner of Column (A) of Figure 4. Several differences compared to Figure 3 are apparent. First, less deformation of the fluid interface is observed in the phase field and pressure contour plots compared to the baseline case. This is a direct result of the electrowetting force being reduced by the shielding of the EP electrode. Secondly, comparison of Column (B) of Figures 3 and 4 reveals differences in the computed velocity field as indicated by the absence of a dark region in the plots
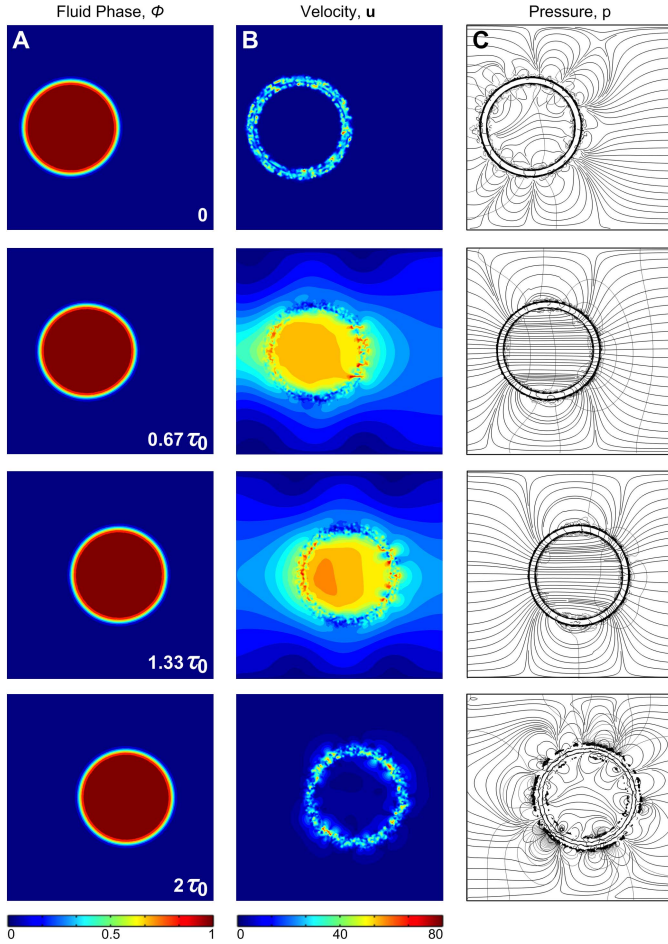
Fig. 4. EP/EWD fluid transport analysis results for $A_{EP}/A_{EW} = 0.75$; ($w = 3L/16$). (A) Fluid phase, ϕ; (B) velocity magnitude, $\|\mathbf{u}\|$, where units in the scale bar below are in mm·s^{-1}; (C) contours of the pressure field, p.

of velocity magnitude in Column (B) of Figure 4. Rather than an advancing front with a smooth velocity profile as observed for the baseline case, five fluid jets are apparent in the velocity profiles for $t = 0.67\tau_0$ and $t = 1.33\tau_0$ for the case where $A_{EP}/A_{EW} = 0.75$. The locations of these jets correlate with the locations where the EWD electrode is unshielded by the EP electrode. Additionally, the pressure contours shown in Figure 4 Column (C) appear more sparse than the baseline case, indicating a pressure gradient of lesser magnitude. Moreover, the characteristic time scale for droplet transport was found to double for the case where $A_{EP}/A_{EW} = 0.75$ compared to baseline.

A series of similar simulations was conducted for a range of values of A_{EP}/A_{EW} to quantify the fluidic effects depicted in Figures 3 and 4. For each simulation, the threshold voltage was determined by incrementing the applied voltage, per the Lippmann Equation (23), and noting the minimal voltage required to generate droplet motion. Additionally, the magnitude of the electrowetting force was computed for each simulation. The magnitude of the electrowetting force may be calculated by integrating the component of the forcing term from Eq. 11 responsible for augmenting the z-curvature of the

droplet interface, as follows.

$$\|\mathbf{F}_{EW}\| = \int_{V} \mathbf{f}_{EW} \cdot \hat{\mathbf{n}}_i d\,V \tag{18}$$

$$= -\int_{V} \kappa_{Hys} \frac{\gamma_{LV} L}{d^2} \kappa_z \hat{\mathbf{n}}_i \cdot \hat{\mathbf{n}}_i d\,V \tag{19}$$

$$\simeq \int_{V} \kappa_{Hys} \frac{\gamma_{LV} L}{d^3} \left[2\cos\theta_Y + \frac{\varepsilon_r \varepsilon_0}{2t\gamma_{LV}} V(\mathbf{x})^2 \right] d\,V \tag{20}$$

Since θ_{EW} is only defined at the contact line, the integral may be assumed to be zero everywhere except the volume that contains the interface. This calculation was completed for each time step, in each simulation to track the force applied by the EWD electrode. Lastly, Reynolds number, from Eq. 23 was computed for each time step to more closely measure fluid velocity and droplet transport time. Reynolds number is defined as the ratio of inertial to viscous forces, as follows:

$$Re = \frac{\rho \|\mathbf{u}\| L}{\mu} \tag{21}$$

For each quantity computed, values relative to the baseline EWD transport process are reported. This method emphasizess the comparative analysis and captures relative device performance, which allows for easier assimilation of the impact of the EP wire on EWD fluid dynamics.

Figure 5 shows the trends in threshold voltage, electrowetting force, and Reynolds number observed for the simulation series. The baseline threshold voltage, $V_{T,0}$ was found to be 24 V. As expected, the EWD threshold voltage was found to increase nonlinearly as A_{EP}/A_{EW} was increased from 0 to 1. Figure 5 (A) shows the points (black squares) computed for threshold voltage, relative to the baseline, $V_T/V_{T,0}$. A value of $V_T/V_{T,0}$ for $A_{EP}/A_{EW} = 1$ was not determined as a singularity in the trend was likely reached. Further analysis revealed the points to be well approximated by the analytical function $(1 - A_{EP}/A_{EW})^{-1/2}$. The dielectric strength of SU-8, a potential EWD dielectric film, is ~ 4.4 MV·cm^{-1} [40]. For reference, the breakdown voltage for a 2 μm SU-8 film is plotted relative to the baseline threshold voltage in Figure 5 (A) as the hatched region at the top of the figure. This comparison demonstrates the electrical tolerance that the EP electrode design offers to EP/EWD integration in terms of fractional area of coverage. As shown in plot, at 50% coverage, the threshold voltage of the EP/EWD device is only increased by a factor of 1.4, which corresponds to only 10% of the breakdown voltage of a 2 μm SU-8 EWD film. This result suggests high feasibility for realization of the device.

The EW force relative to the unshielded baseline, F/F_0 was computed for each simulation per the volume integral shown in Eq. 20. Figure 5 (B) shows the values computed for F/F_0 as black squares. The inset shows the relative EW force tracked through time for three different simulations, where A_{EP}/A_{EW} was set to 0 (dark blue diagonal hatch), 0.5 (dark blue), and 0.75 (light blue horizontal hatch). Separately, the relative EWD force was estimated numerically by integrating the logical expression $(\theta(x, y) < \theta_Y)$, which equals unity in regions of the contact line where the EWD electrode is unshielded and
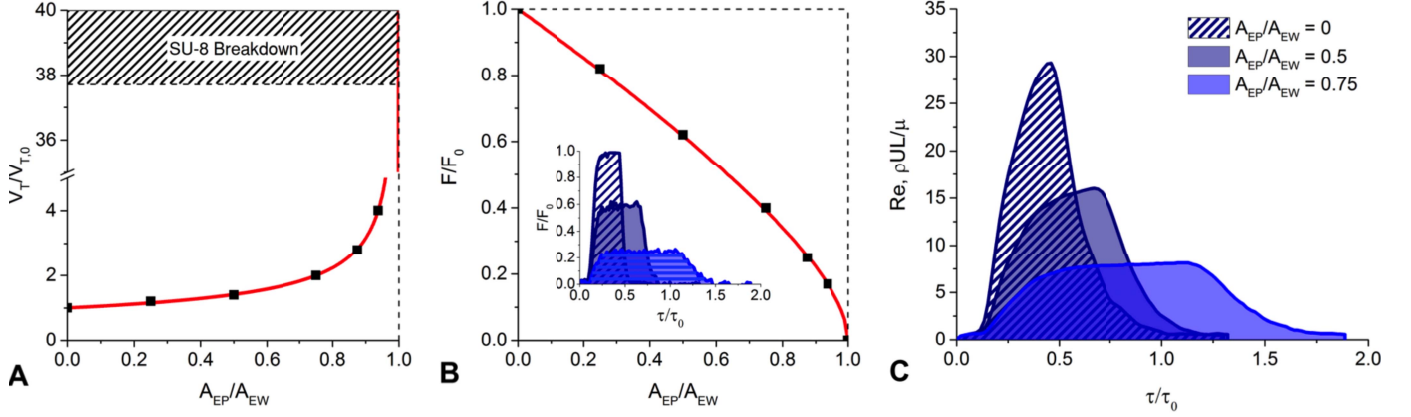
Fig. 5. Summary of the fluid transport analysis. (A) Threshold voltage, relative to the baseline, $V_T/V_{T,0}$ versus fractional area of coverage, A_{EP}/A_{EW} (black squares) plotted with a trendline, $(1 - A_{EP}/A_{EW})^{-1/2}$ (solid, red line). (B) Electrowetting force relative to the baseline case versus A_{EP}/A_{EW} (black squares) plotted with the trendline numerically computed in Eq. 22; (Inset) Relative EW force tracked through time for three different simulations, where A_{EP}/A_{EW} was set to 0 (dark blue diagonal hatch), 0.5 (dark blue diagonal hatch), and 0.75 (light blue horizontal hatch). (C) Reynolds number tracked through time for three different simulations, where A_{EP}/A_{EW} was set to 0 (hatch), 0.5 (dark blue), and 0.75 (light blue horizontal hatch).

zero otherwise.

$$F/F_0 \simeq \frac{\| \oint_{CL} (\theta(x,y) < \theta_Y) \, \hat{\mathbf{n}}_i \, dl \|}{\| \oint_{CL} (\theta_0(x,y) < \theta_Y) \, \hat{\mathbf{n}}_i \, dl \|} \qquad (22)$$

where, $\theta(x,y)$ is the scalar field mapping of the electrowetting angle for arbitrary values of A_{EP}/A_{EW}, and $\theta_0(x,y)$ is the baseline scenario as depicted in Figure 2. This approach was found to closely approximate the values of F/F_0 computed in the numerical simulation and is plotted as the red line in Figure 5(B).

Lastly, Figure 5 (C) shows Reynolds numbers computed for three cases, where $A_{EP}/A_{EW} = 0$ (hatch), 0.5 (dark blue), and 0.75 (light blue). In these cases, Reynolds number is used as a proxy for velocity magnitude. Figure 5 (C) shows that as A_{EP}/A_{EW} increases, droplet actuation is slowed significantly. This retarding effect has a direct impact on the droplet transport time, which is clearly demonstrated in Figure 5 (C). In the baseline case, Re jumps quickly to its peak value of 30 as the droplet accelerates toward the unshielded electrode. As the majority of the droplet moves onto the electrode, Re begins a slow decay to its quiescent value by $t = \tau_0$. For cases where $A_{EP}/A_{EW} > 0$, values of Re are reduced in peak value, but stretched over time indicating a slow moving droplet taking longer to move onto the energized EWD electrode. The case of complete coverage, where $A_{EP}/A_{EW} = 1$, Re remained at its quiescent value and the transport time was assumed to be ∞.

The EP/EWD device model describes the impact of the EP electrode on EW dynamics. The geometry of the EP/EWD device was parameterized by the ratio of EP device area to the area of the EWD device, A_{EP}/A_{EW}, and used in comparisons of the actuation performance of the integrated EP/EWD device for different parameter values. Important EWD actuation parameters including threshold voltage, EW force, droplet velocity, and transport time were computed for several values of the geometric parameter, A_{EP}/A_{EW}. Threshold voltage and transport time were found to increase to ∞ as A_{EP}/A_{EW} was increased from 0 to 1. Meanwhile, the

EW force and the Reynolds number were found to decrease to zero and the Re quiescent value, respectively, as coverage of the EP wire was increased to 100%. These results suggest that conservative designs should limit A_{EP}/A_{EW} to <0.5.

V. EXPERIMENTAL METHODS

We measured the following three parameters associated with droplet transport in the EP/EWD device: threshold voltage (V_T), transport time (τ), and actuation velocity (U). These transport parameters were measured for cases where the EP electrode was present and absent. Cases in which the EP was absent were used to assess baseline EWD performance, since this condition reflects typical, unobstructed EWD operation. Thus, the baseline EWD transport parameters are controls in an experiment, which has the objective of characterizing droplet transport in the integrated EP/EWD device geometry.

Further, the following experiments test a two-part hypothesis regarding fluid transport in the proposed EP/EWD device. It is hypothesized that (1) the presence of the EP electrode significantly impedes droplet transport, but (2) this impediment can be overcome by moderately increasing the EWD voltage by a an amount that will not result in catastrophic device failure. The fluid transport model developed in Section III predicts that a 25% increase in threshold voltage will be required to restore droplet actuation over the EP wire, and that compared to the baseline case the EP/EWD device will exhibit a 20% increase in transport time, and a 15% decrease in actuation velocity.

A. Device Fabrication

1) Bottom Plates: Typical EWD microfabrication methods were used to batch-produce EP/EWD devices as previously described [41]. EP/EWD bottom plates were fabricated on 100 mm diameter, 1 mm thick borosilicate glass wafers. The EWD electrode layer was patterned in ITO (10 $\Omega \cdot$ sq^{-1}) by University Wafer, Inc.

The EW dielectric film was formed by spinning SU-8 2002 (MicroChem, Inc.) to a thickness of 2 μm. A two-stage pre-exposure bake (PEB) was conducted at 65 °C for 1 min followed by 95 °C for 2 mins. Windows to the EWD I/O electrical contact pads were opened by patterning the SU-8 with the MA6 Frontside/Backside Mask Aligner (Süss MicroTec) and a bright field mask (International Phototool Company, LLC). Samples were exposed with a dose of 150 mJ·cm^{-2}. The samples were then baked at 65 °C for 1 min followed by 95 °C for 2 mins and developed in SU developer (MicroChem, Inc.) for 1 min after cooling to room temperature. After development, the SU-8 film was then hard baked at 180 °C for 30 mins. After patterning the EW dielectric film, samples were surface ashed at 100 W in an oxygen plasma for 90 s to remove any surface residues.

The EP electrode was formed using a simple liftoff method with negative photoresist and a 5:200 nm Ti:Au film. In preparation for the EP electrode film, an oxide adhesion layer was deposited onto the EW dielectric by shadow masking the exposed EWD I/O contact pads with low tack tape (Ultron Systems, Inc.) and depositing 20 nm of SiO_2 in an RF dielectric sputter system (Kurt J. Lesker PVD 75). The low tack tape was removed and the wafers were cleaned with acetone and IPA. A 3.9±0.1 μm flim of negative photoresist (NFR 016 D2, JSR Micro, Inc.) was spun onto the substrates and a PEB was conducted at 90 °C for 3 min on a level hotplate. Subsequently, a brightfield mask (International Phototool Company, LLC) of the EP electrode pattern was used with the MA6 Frontside/Backside Mask Aligner (Süss MicroTec) to pattern the negative photoresist. After exposure, the photoresist was developed in MF-319 Shipley Microposit® developer for 1 min. Next, a 5:200 nm Ti:Au film was deposited onto the wafers with an electron-beam metal evaporator (CHA Industries, Inc.). Wafers were then submerged in acetone for 3 hr to dissolve the photoresist and liftoff regions the the metal film unbound to the wafer surface. After the acetone soak, samples were agitated with a disposable pipette, cleaned with acetone and IPA, and finally dried with compressed N_2.

Following the pattern transfer of the EP device layer, a protective coat of positive photoresist (Shipley Microposit® S1813) was spun onto the wafer at 3,000 rpm for 30 s and baked at 115 °C for 1 min. Samples were then transferred to ring-tensioned low tack tape and mounted in a dicing saw (DAD3220, Disco, Inc.). A total of 9 cuts were made, 5 in the x-direction and 4 in y, yielding 8 chips from each 100 mm wafer. EWD gaskets were fabricated out of 0.005" (127 μm) Duralar polyester with adhesive backing (Grafix Plastics, Inc.). The gasket layout was designed with 2D AutoCAD drafting software (AutoDesk, Inc.) and cut out using a CO_2 laser cutting system (VLS 6.60, Universal Laser Systems). The parameters used to cut the polyester film with minimal melting, burning, or deformation, included 25% laser power, 25% translation speed, and a focal position of 0.007" (178 μm).

After the gaskets were laser cut, they were cleaned with an IPA-dampened swab and dried with compressed N_2. Gaskets were then manually aligned and applied to the diced chips

under a stereoscopic microscope. After the gaskets were applied, the EWD I/O and EP (+) contacts on each chip were masked with strips of low tack tape (Ultron Systems, Inc.). An amorphous fluoropolymer hydrophobic layer, 20% wt. CYTOP (Bellex International Corp.), was spun onto the chips at 2500 rpm for 30 s, producing a 70 nm thick film. Finally, the low tack tape was removed and the CYTOP film was heat-cured by baking at 180 °C for 30 mins, completing the microfabrication of the EP/EWD bottom plate.

2) Top Plates: The EP/EWD top plates were machined out of 1/8" thick polycarbonate sheet stock (McMaster-Carr). A 6×6" slab of PC was mounted onto a sacrificial plate affixed to a CNC end mill stage (Roland Modela: MDX-20) with 3M double-sided tape (McMaster-Carr). A pattern corresponding to the top plate outline and pipette inlets was designed using AutoCAD 2013 3D drafting software (AutoDesk, Inc.) and used to produce stereolithography (STL) files, needed for milling the sheet stock. First, a 1/8" (3.175 mm) diameter (1/8" shank), square-end, four-flute carbide end mill (McMaster-Carr) was used to mill the oil reservoirs and top plate outline in the PC stock. Then, a 1/32" (800 μm) diameter (1/8" shank), square-end, four-flute carbide end mill (McMaster-Carr) was used to mill the pipette inlet through holes within the oil reservoirs.

After the top plate geometry was machined, the top plates were immersed in a 1% Alconox cleaning solution (Alconox, Inc.) and sonicated at 100 W for 5 mins. The top plates were then immersed in DI water and sonicated again for 5 mins before being rinsed with IPA and dried with compressed N_2. Clean substrates were transferred onto the sample holder of the Kurt J. Lesker PVD 75 RF dielectric sputter system (Kurt J. Lesker Co.) and placed into the vacuum chamber of the sputter tool. The vacuum chamber was pumped down to a pressure of 10^{-7} Torr and, 50 nm of ITO was deposited onto the plastic substrates. During the deposition, the turbo pump was set to 50% maximum speed; Ar gas pressure was set to 15 mTorr; and an RF power of 120 W was applied to the ITO target. Deposition time was approximately 45 mins.

After ITO deposition, low tack tape (Ultron Systems, Inc.) was applied to the lateral edges of the top plate and an amorphous fluoropolymer hydrophobic layer, 20% wt. CYTOP (Bellex International Corp.), was spun onto the chips at 2500 rpm for 30 s, producing a ~70 nm thick film. The low tack tape served as a shadow mask for regions where electrical contact to the ground plane will be made during device testing. The low tack tape was removed and the top plates were baked at 60 °C for 12 hrs.

B. EP/EWD Chip Staging

The devices included an EWD electrode pitch of 700 μm and an EP electrode width of 60 μm, which imparted a fractional area of coverage, A_{EP}/A_{EW}, of 0.34. Individual EWD chips were loaded into the EP/EWD test apparatus described in [41]–[43]. The EWD control system comprised 1) a waveform generator and 10× voltage amplifier for EWD signal generation; 2) a high-voltage relay board equipped with a microcontroller for EWD signal routing and interfacing with

a custom GUI for user control; and 3) a spring loaded 22-pin IC test clip for making contact to the EWD chip via a ribbon connector. The IC test clip and loading spring were mounted into a polycarbonate base plate and used to hold a) the EWD chips in place during testing and b) make electrical contact to the on-chip EWD electrodes. Microscope stage clips were fixed to the base plate with thumb screws and used to hold the EWD top plates to the mounted bottom plates. With the top and bottom plates mounted, aligator clips were attached to the extents of the top plate to provide an electrical ground to the top plate. A CCD camera and telephoto lens mounted beneath the EWD stage allowed real-time microscopic imagery of the device during each test. After the chips were mounted, electrical connections to the bottom and top plate were made by attaching a ribbon connector to the test clip and the EWD ground (alligator clip) to the lateral side of the bottom plate.

C. Fluid Input

Once the EP/EWD chips were set in place and the electrical connections established, approximately 25 μL of 2 cSt silicone oil was added to the EWD devices with a P200 micropipette via the pipette inlets near the fluid reservoirs. The EW voltage was set to a 1 kHz, 40 V_{p-p} sine wave and a custom EWD control user interface was used to energize all four EWD electrodes in the reservoir on one side of the EP/EWD device. With the EWD reservoir electrodes activated, 2 μL of a suspension of EcNR2 *E. coli* with an OD_{600} of 3.34 ± 0.15 ($2.67 \pm 1.2 \times 10^9$ cells/mL) and 0.05% Tween 20 (CAS 9005-64-5, Sigma-Aldrich Co.) in nuclease free water were pipetted into the EWD reservoir with a P10 micropipette.

D. Droplet Generation and Actuation

With the silicone oil and EcNR2 cells loaded into the device, 2$\times$ droplets of cells, approximately 200 nL in volume, were dispensed onto the EWD electrode array in the following way. Two reservoir electrodes closest to the channel and four channel electrodes were activated causing the cell-containing fluid to wet into the channel and form a finger-shaped interface. Once the fluid interface stabilized, the two center channel electrodes were deactivated causing the center of the finger-shaped interface to narrow and eventually collapse. This actuation sequence resulted in a bolus of fluid held on the two activated reservoir electrodes and a 2$\times$ droplet of fluid held in place on the two activated channel electrodes.

After the droplets were dispensed, the actuation voltage was decreased to a sub-threshold value, typically 25 Vp-p. An electrode adjacent to the position of the droplet was then actuated and the holding electrode was deactivated. The actuation voltage was increased in increments of 1 V and the previous step repeated until droplet transport was observed. The minimum voltage required to cause droplet transport was recorded as the threshold voltage. To establish the baseline EWD operation, this procedure was conducted on channel electrodes where the EP wire was absent. After measuring the baseline threshold voltage, droplets were actuated to the EP/EWD electrode, and the previous procedure was repeated to determine the threshold voltage of the EP/EWD device.

Once the EP/EWD threshold voltage was measured, droplets were actuated with the new threshold voltage on channel electrodes while image sequences of the droplet motion were captured at 30 fps. Subsequently, droplets were actuated on the EP/EWD electrode and similar image sequences were recorded. Images of the droplet transport were analyzed to determine the transport time and average actuation velocity for both the baseline and EP/EWD cases. Transport time was defined as the time required to translate the droplet centroid by 1 electrode pitch, 700 μm. Actuation velocity was calculated as the quotient of the electrode pitch and the transport time. Transport parameters were measured on 16 different chips generated in two independent fabrication runs.

E. Post-Pulse Actuation

As reported elsewhere, EP experiments were conducted in concert with the previousl described actuation experiments [41]. To assess stability and reproducibility, more than 10 EP experiments were carried out on each device. The EP experiments consisted of exposing droplets and underlying fluoropolymer layers to electric field pulses that ranged in strength from 0 to 3 kV·mm^{-1}; each applied pulse had a time constant of 6 ms and a decaying exponential pulse shape. After each pulse, video of droplet transport was recorded at 30 fps and analyzed for any deviation from baseline behavior.

VI. Experimental Results

A. Typical EWD Transport

A sequence of the images captured for the baseline EWD actuation case is shown in Figure 6 (column A) alongside predictions of the shape of the fluid interface (column B) and the fluid velocity field (column C). The image sequence in Figure 6 (A) shows deformation of the fluid interface and droplet translocation that are indicative of typical EWD dynamics and within reasonable agreement of respective theoretical results.

The 2$\times$ droplet, which was held on two electrodes, is initially at rest. As the neighboring electrodes are activated, the wetting angle of the adjacent contact line is reduced and a pressure differential develops across the droplet causing the droplet to accelerate toward the energized EWD electrode. The fluid interface deforms in response to stresses generated by the electrowetting force. The baseline EWD threshold voltage was experimentally measured to be 35 ± 4 V ($\mu \pm \sigma$). Additionally, results from the image analysis indicate baseline transport time and actuation velocity to be 0.280 ± 0.030 s and 2.5 ± 0.3 mm/s, respectively.

B. EP/EWD Transport

A sequence of the images captured for the actuation of a droplet over the EP/EWD electrode is shown in column A of Figure 7. Predictions of the shape of the fluid interface (B) and the fluid velocity field (C) agree with experimental results. The image sequence depicts a deformation of the fluid interface characteristic of nonuniform electrowetting. Rather than the entire advancing contact line wetting uniformly, a small
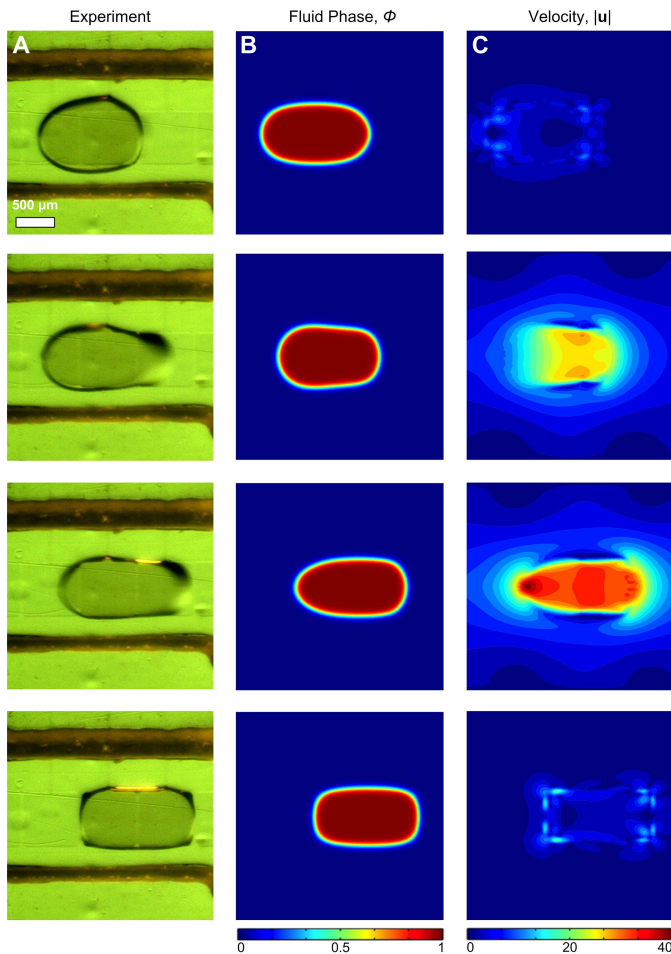
Fig. 6. Experimental and Theoretical Results for Baseline EWD Transport. (A) Typical droplet transport over completely unshielded EWD electrode. The scale bar indicates 500 μm. (B) Theoretical predictions of the fluid interface, or phase, for typical EWD actuation. (C) Theoretical predictions of the velocity magnitude field for typical EWD actuation.
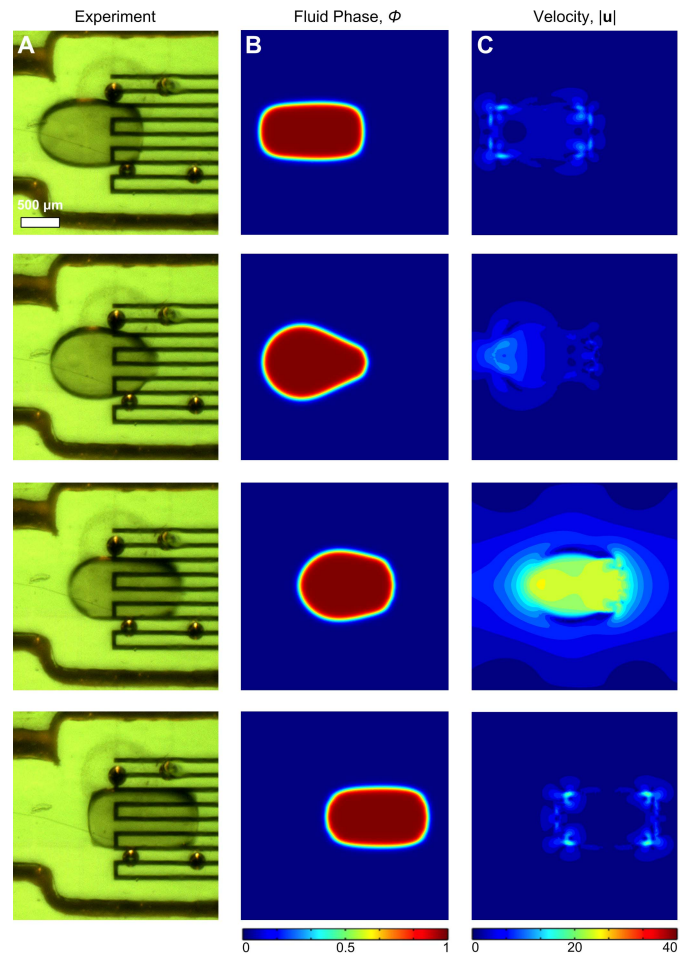
Fig. 7. Experimental and Theoretical Results for Droplet Transport in the EP/EWD Device; ($w = 0.086L$; A_{EP}/A_{EW}=0.34). (A) Droplet transport over EP/EWD electrode. The scale bar indicates 500 μm. (B) Prediction of the fluid interface during actuation over the EP/EWD electrode. (C) Prediction of the velocity magnitude field for actuation over the EP/EWD electrode.

portion of the contact line is modulated during the initiation of droplet motion. The small portion of the affected contact line results in fluid stress that compress the sides of the droplet causing it to assume a pear-shaped bolus. Moreover, the reduced area of the actuated electrode results in a reduction of the total electrowetting force compared to the baseline case, which is observed as slower droplet transport.

The threshold voltage of the EP/EWD device was measured to be 45 ± 6 V, and the transport time and actuation velocity were measured to be 0.510 ± 0.100 s and 1.4 ± 0.3 mm/s, respectively. Results from droplet transport over the EP/EWD electrode are summarized in Table II. No dielectric breakdown (*e.g.* hydrolysis, catastrophic device failure, rapid oxidation, *etc.*) or noticeable charging, as measured as a drift in threshold voltage of the EP/EWD device, was observed in response to the increased EW voltage operation required for droplet transport over the EP/EWD device.[1] During droplet actuation, we estimate the nominal electric field in the EW dielectric to be on the order of 0.18 MV·cm^{-1} and 0.23 MV·cm^{-1} for the

---

[1]Gas bubbles observed in Figure 7 (A) were the result from tests of the EP pulse operation and not droplet actuation.

TABLE II
EP/EWD TRANSPORT SUMMARY

Device	Threshold Voltage V_{T} (V)	Transport Time τ (s)	Average Velocity $\overline{U}$ (mm/s)
EWD	35 ± 4	0.28 ± 0.03	2.5 ± 0.3
EP/EWD	45 ± 6	0.51 ± 0.10	1.4 ± 0.3
Percent Change, Δ	29%	82%	-44%

Values reported for each parameter are $\mu \pm \sigma$ for 6 separate devices.

baseline and EP/EWD cases, respectively. Electromechanical models, which take into account electric field intensification due to induced charge density near the droplet contact line, suggest peak electric field strengths within the EW dielectric to be on the order of 10 times greater than that of the nominal field [44], [45]. Estimated values of the peak electric field near the droplet contact line correspond to 40% and 50% of the dielectric strength of the SU-8 EWD dielectric for the baseline and EP/EWD cases, respectively. Hence, we did not expect nor did we observe any instances of dielectric breakdown of the SU-8 dielectric during droplet actuation.
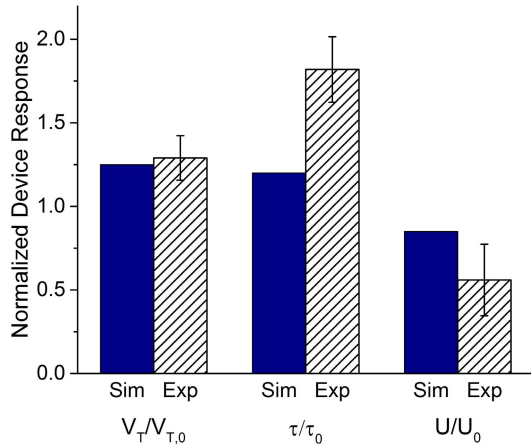
Fig. 8. Summary of Theoretical and Experimental Results of the EP/EWD Device. Normalized threshold voltage, $V_T/V_{T,0}$, transport time, τ/τ_0, and average transport velocity, $\overline{U}/\overline{U_0}$, for the EP/EWD device are plotted for theoretically (Sim) and experimentally (Exp) determined cases.

An additional comparison of baseline EWD performance to the integrated EP/EWD device was accomplished by normalizing the theoretical and experimentally determined values of the fluid transport parameters, V_T, τ, and $\overline{U}$, to their respective baseline values. Normalized threshold voltage, transport time, and average transport velocity for the EP/EWD device were respectively computed for simulated and experimentally determined values as $V_T/V_{T,0}$, τ/τ_0, and $\overline{U}/\overline{U_0}$, where the subscript 0 indicates the baseline, unshielded fluid parameter.

Normalized threshold voltage, transport time, and average transport velocity computed with the fluid transport model were found to be 1.25, 1.2, and 0.85. Meanwhile, corresponding values were experimentally determined to be 1.29±0.13, 1.82±0.20, and 0.56±0.21. Figure 8 shows a bar chart which compares the theoretical (Sim) and experimentally (Exp) determined values of the normalized fluid transport parameters for the EP/EWD device. The normalization of computed and experimentally determined transport parameters enables the comparison of 1) device operation in the presence and absence of the integrated EP electrode and 2) the performance of the model to experimental observation. Highlights of these comparisons are discussed in the following section.

C. Device Stability

A few critical observations were made with respect to EP pulse-induced changes to droplet transport in the EP/EWD device. Mild EP pulses, less than 1 kV·mm^{-1}, had no noticable impact on droplet transport dynamics, whereas EP pulses of sufficient strength ($1 < \|\mathbf{E}_{EP}\| < 2$ kV·mm^{-1}) were found to impede, but not hault droplet transport. In extreme cases, where the strength of EP pulse was greater than 2 kV·mm^{-1}), droplet hydrolysis, contact line pinning, and dielectric breakdown were observed in as little as a single EP pulse. These results suggest that moderate to intense EP pulses can cause instability and failure modes within the EWD dielectric and fluoropolymer layers. Greater detail of EP pulse-induced failure modes in the EP/EWD device are reported elsewhere [41].

VII. DISCUSSION

The integrated EP/EWD device was found to support droplet transport at an elevated EW threshold voltage without exhibiting signs of catastrophic device failure such as dielectric breakdown. Furthermore, theoretical predictions and experimental observations showed agreement within reasonable operating margins of threshold voltage, transport time, and average transport velocity. The fluid transport model developed in Section IV predicted that the presence of a metal layer shielding 34% of the underlying EWD electrode would require a 25% increase in threshold voltage compared to the EP wire-free case. For the same device geometry, the transport model predicted the EP/EWD device to exhibit a 20% increase in transport time, and a 15% decrease in actuation velocity.

The presence of the partially shielding EP layer was hypothesized to significantly impede droplet transport due to electric field screening of the droplet contact line from the underlying EWD electrode. However, it was predicted that this impediment could be overcome by increasing the EWD voltage to a value that would restore droplet transport without causing catastrophic damage to the EW dielectric. It is important that this compensation is not valid for all geometries, especially since the threshold voltage for a partially shielded EWD electrode is predicted to increase nonlinearly with the fractional area of coverage, $A_{EP/A_{EW}}$, as $V_T = V_{T,0} \left(1 - A_{EP/A_{EW}}\right)^{-1/2}$. The extent to which the actuation voltage may be compensated for partial EWD shielding relies heavily on the fractional area of coverage, the strength, quality, and thickness of the EW dielectric and fluoropolymer layers, as well as the interfacial surface tension, and any fluidic barriers to transport such as hysteresis angle and pinning sites on the actuator surface.

As summarized in Table II, the fluid transport model was capable of predicting threshold voltage within 6 V, transport time within 0.39 ms, and actuation velocity within 0.9 mm/s. The threshold voltage, transport time, and actuation velocity were found to change by 29%, 82%, and −44%, respectively. Compared to the predicted parameters, the observed transport parameters reflect percent differences of 3.1%, 41%, and 41%, respectively. These discrepancies are likely due to estimation of key physical parameters and omission of more complicated terms in the Navier-Stokes formulation of the forcing term shown in Eq. 11. The effects of the 0.05% Tween-20 surfactant as well as the presence of the *E. coli* cell suspension on fluid transport parameters were not captured in the numerical model. Effective fluid viscosity, μ, zero voltage wetting angle, θ_Y, surface tension, σ, and hysteresis angle, α, of the tween-20 and cell suspension in an oil medium were each estimated. Additionally, the EW wetting angle, $\theta(V)$ was calculated using the Young-Lippman equation, Eq. 23. The accuracy of transport model would likely improve if these parameters were measured on similar substrates rather than assuming approximate values, as was done in this study.

In addition to the estimation of key fluid parameters, our model does not account for the electric field distribution inside of the EW dielectric. While the estimation of the $\hat{z}$-curvature of the droplet interface greatly simplifies the transport problem, our approach relies on the assumption that 1) the electric field distribution within the EW dielectric is

uniform and 2) that the droplet contact angle will be reduced only in areas not shielded by the EP electrodes. However, the interaction between the electric field and the droplet interface must be simulated in order to precisely predict the extent of contact angle reduction. This deficiency may further explain the differences between our theoretical and experimental results.

The presence of surfactants and cells in a fluid of interest presents a considerable modeling challenge as each entity imparts effective fluid parameters that are notoriously difficult to capture in a few physical parameters. Furthermore, coupling of the electric field distribution in the EWD dielectric and droplet interface dynamics will require a higher dimension computation. Correcting these deficiencies would certainly produce a more rigorous model but, the deviation between experiment and theory of the EP/EWD device operation is minimal with respect to device operability. The EW force was predicted to drive droplet motion despite significant electric shielding from an integrated EP structure, precisely what was observed.

VIII. Conclusion

The operability of a partially shielded EP/EWD device has been verified both theoretically and experimentally. The standard Navaier-Stokes formulation was implemented in conjunction with a straightforward treatment of the electrowetting force resulting from the activation of a partially shielded EWD electrode. Basic fluidic experiments on in-house fabricated devices performed as expected. Droplet actuation was found to be supported by the integrated device. However, an increased threshold voltage was required to maintain fluid transport in the partially shielded device compared to an unshielded EWD actuator of similar construction. The present work applies established modeling principles and basic experimental technique to assess the utility of an architecture that integrates fluid handling and gene transfer capabilities into a single, scalable device.

Appendix A
The Young-Lippmann Equation

An electric potential, V, applied between a liquid droplet and the supporting electrode results in the formation of a localized electric field across the underlying insulator. This gives rise to an electrowetting force which reduces the macroscopic contact angle of the droplet and drives droplet actuation [14], [38], [39]. The Young-Lippmann equation (Eq. 23) is frequently used to describe the mechanism of EWD actuation:

$$\cos\theta_{\text{EW}} = \cos\theta_{\text{Y}} + \frac{\varepsilon_{\text{r}}\varepsilon_0}{2t\,\gamma_{\text{LV}}}V^2 = \cos\theta_{\text{Y}} + \eta \qquad (23)$$

where θ_{EW} is the voltage-dependent electrowetting contact angle, θ_Y is Young's angle of the system at zero voltage, t is the thickness of the dielectric with permittivity, $\varepsilon\varepsilon_0$, and γ_{LV} is the interfacial tension between the droplet and the surrounding medium, and η is the electrowetting number.

References

[1] G. Lippmann, "Relations entre les phénomènes électriques et capillaires," *Ann. Rev. Chim. Phys.*, vol. 5, p. 494, Jan. 1875.

[2] M. G. Pollack, R. B. Fair, and A. D. Shenderov, "Electrowetting-based actuation of liquid droplets for microfluidic applications," *Appl. Phys. Lett.*, vol. 77, no. 11, pp. 1725–1726, 2000.

[3] R. B. Fair, A. Khlystov, V. Srinivasan, V. K. Pamula, and K. N. Weaver, "Integrated chemical/biochemical sample collection, pre-concentration, and analysis on a digital microfluidic lab-on-a-chip platform," *Proc. SPIE*, vol. 5591, pp. 113–124, Dec. 2004.

[4] V. Srinivasan, V. K. Pamula, and R. B. Fair, "An integrated digital microfluidic lab-on-a-chip for clinical diagnostics on human physiological fluids," *Lab Chip*, vol. 4, no. 4, pp. 310–315, May 2004.

[5] R. B. Fair, "Digital microfluidics: Is a true lab-on-a-chip possible?" *Microfluidics Nanofluidics*, vol. 3, pp. 245–281, Jun. 2007.

[6] A. R. Wheeler, "Putting electrowetting to work," *Science*, vol. 322, no. 5901, pp. 539–540, 2008.

[7] A. R. Wheeler, H. Moon, C.-J. Kim, J. A. Loo, and R. L. Garrell, "Electrowetting-based microfluidics for analysis of peptides and proteins by matrix-assisted laser desorption/ionization mass spectrometry," *Anal. Chem.*, vol. 76, no. 16, pp. 4833–4838, 2004.

[8] S. K. Cho, H. Moon, and C.-J. Kim, "Creating, transporting, cutting, and merging liquid droplets by electrowetting-based actuation for digital microfluidic circuits," *J. Microelectromech. Syst.*, vol. 12, no. 1, pp. 70–80, Feb. 2003.

[9] B. Berge and J. Peseux, "Variable focal lens controlled by an external voltage: An application of electrowetting," *Eur. Phys. J.*, vol. 3, no. 2, pp. 159–163, Oct. 2000.

[10] R. A. Hayes and B. J. Feenstra, "Video-speed electronic paper based on electrowetting," *Nature*, vol. 425, no. 6956, pp. 383–385, 2003.

[11] H. You and A. J. Steckl, "Three-color electrowetting display device for electronic paper," *Appl. Phys. Lett.*, vol. 97, no. 2, p. 023514, 2010.

[12] B. E. White, Jr., "Energy-harvesting devices: Beyond the battery," *Nature Nanotechnol.*, vol. 3, no. 2, pp. 71–72, 2008.

[13] F. Mugele and J.-C. Baret, "Electrowetting: From basics to applications," *J. Phys., Condens. Matter*, vol. 17, no. 28, pp. 705–774, 2005.

[14] F. Mugele, "Fundamental challenges in electrowetting: From equilibrium shapes to contact angle saturation and drop dynamics," *Soft Matter*, vol. 5, no. 18, pp. 3377–3384, 2009.

[15] J. H. Song, R. Evans, Y.-Y. Lin, B.-N. Hsu, and R. B. Fair, "A scaling model for electrowetting-on-dielectric microfluidic actuators," *Microfluidics Nanofluidics*, vol. 7, no. 1, pp. 75–89, 2009.

[16] H. Ren, R. B. Fair, M. G. Pollack, and E. J. Shaughnessy, "Dynamics of electro-wetting droplet transport," *Sens. Actuators B, Chem.*, vol. 87, no. 1, pp. 201–206, 2002.

[17] S. W. Walker and B. Shapiro, "Modeling the fluid dynamics of electrowetting on dielectric (EWOD)," *J. Micromech. Syst.*, vol. 15, no. 4, pp. 986–1000, 2006.

[18] S. W. Walker, B. Shapiro, and R. H. Nochetto, "Electrowetting with contact line pinning: Computational modeling and comparisons with experiments," *Phys. Fluids*, vol. 21, no. 10, p. 102103, 2009.

[19] A. G. Papathanasiou and A. G. Boudouvis, "Manifestation of the connection between dielectric breakdown strength and contact angle saturation in electrowetting," *Appl. Phys. Lett.*, vol. 86, no. 16, p. 164102, 2005.

[20] V. Peykov, A. Quinn, and J. Ralston, "Electrowetting: A model for contact-angle saturation," *Colloid Polym. Sci.*, vol. 278, no. 8, pp. 789–793, 2000.

[21] H. Ding *et al.*, "Accurate dispensing of volatile reagents on demand for chemical reactions in EWOD chips," *Lab Chip*, vol. 12, no. 18, pp. 3331–3340, 2012.

[22] H. Norian, R. M. Field, I. Kymissis, and K. L. Shepard, "An integrated CMOS quantitative-polymerase-chain-reaction lab-on-chip for point-of-care diagnostics," *Lab Chip*, vol. 14, no. 20, pp. 4076–4084, 2014.

[23] Y.-H. Chang, G.-B. Lee, F.-C. Huang, Y.-Y. Chen, and J.-L. Lin, "Integrated polymerase chain reaction chips utilizing digital microfluidics," *Biomed. Microdevices*, vol. 8, no. 3, pp. 215–225, 2006.

[24] W. C. Nelson, I. Peng, G.-A. Lee, R. L. Loo, R. L. Garrell, and C.-J. Kim, "Incubated protein reduction and digestion on an electrowetting-on-dielectric digital microfluidic chip for MALDI-MS," *Anal. Chem.*, vol. 82, no. 23, pp. 9932–9937, 2010.

[25] S. H. Au, S. C. C. Shih, and A. R. Wheeler, "Integrated microbioreactor for culture and analysis of bacteria, algae and yeast," *Biomed. Microdevices*, vol. 13, no. 1, pp. 41–50, 2011.

[26] D. G. Pyne, W. M. Salman, M. Abdelgawad, and Y. Sun, "Partially filled electrodes for digital microfluidic devices," *Appl. Phys. Lett.*, vol. 103, no. 2, pp. 024103-1–024103-4, 2013.

[27] T. Lederer, S. Clara, B. Jakoby, and W. Hilber, "Integration of impedance spectroscopy sensors in a digital microfluidic platform," *Microsyst. Technol.*, vol. 18, no. 7, pp. 1163–1180, 2012.

[28] S. K. Cho, Y. Zhao, and C.-J. Kim, "Concentration and binary separation of micro particles for droplet-based digital microfluidics," *Lab Chip*, vol. 7, no. 4, pp. 490–498, 2007.

[29] L. Chen and R. B. Fair, "Digital microfluidics chip with integrated intra-droplet magnetic bead manipulation," *Microfluidics Nanofluidics*, vol. 19, no. 6, pp. 1349–1361, 2015.

[30] I. Barbulovic-Nad, S. H. Au, and A. R. Wheeler, "A microfluidic platform for complete mammalian cell culture," *Lab Chip*, vol. 10, no. 12, pp. 1536–1542, 2010.

[31] K. Choi, J.-Y. Kim, J.-H. Ahn, J.-M. Choi, M. Im, and Y.-K. Choi, "Integration of field effect transistor-based biosensors with a digital microfluidic device for a lab-on-a-chip application," *Lab Chip*, vol. 12, no. 8, pp. 1533–1539, 2012.

[32] L. Malic, T. Veres, and M. Tabrizian, "Two-dimensional droplet-based surface plasmon resonance imaging using electrowetting-on-dielectric microfluidics," *Lab Chip*, vol. 9, no. 3, pp. 473–475, 2009.

[33] L. Malic, T. Veres, and M. Tabrizian, "Biochip functionalization using electrowetting-on-dielectric digital microfluidics for surface plasmon resonance imaging detection of dna hybridization," *Biosensors Bioelectron.*, vol. 24, no. 7, pp. 2218–2224, 2009.

[34] M. Sandahl *et al.*, "Software automated genomic engineering (SAGE) enabled by electrowetting-on-dielectric digital microfluidics," in *Proc. 17th Int. Conf. Miniaturized Syst. Chem. Life Sci. (µTAS)*, Freiburg, Germany, Oct. 2013, pp. 1260–1264.

[35] W. C. Nelson and C.-J. Kim, "Droplet actuation by electrowetting-on-dielectric (EWOD): A review," *J. Adhes. Sci. Technol.*, vol. 26, pp. 1747–1771, May 2012.

[36] E. Olsson and G. Kreiss, "A conservative level set method for two phase flow," *J. Comput. Phys.*, vol. 210, no. 1, pp. 225–246, 2005.

[37] G. K. Batchelor, *An Introduction to Fluid Dynamics*. New York, NY, USA: Cambridge Univ. Press, 1967.

[38] M. G. Pollack, A. D. Shenderov, and R. B. Fair, "Electrowetting-based actuation of droplets for integrated microfluidics," *Lab Chip*, vol. 2, no. 2, pp. 96–101, 2002.

[39] F. Mugele, J.-C. Baret, and D. Steinhauser, "Microfluidic mixing through electrowetting-induced droplet oscillations," *Appl. Phys. Lett.*, vol. 88, no. 20, pp. 204106-1–204106-3, 2006.

[40] J. Melai, C. Salm, S. Smits, J. Visschers, and J. Schmitz, "The electrical conduction and dielectric strength of SU-8," *J. Micromech. Microeng.*, vol. 19, no. 6, pp. 1–7, 2009.

[41] A. C. Madison, "Scalable genome engineering in electrowetting on dielectric digital microfluidic systems," Ph.D. dissertation, Dept. Elect. Comput. Eng., Duke Univ., Durham, NC, USA, Jul. 2015. [Online]. Available: http://search.proquest.com/docview/1718503132

[42] Y.-Y. Lin, E. R. F. Welch, and R. B. Fair, "Low voltage picoliter droplet manipulation utilizing electrowetting-on-dielectric platforms," *Sens. Actuators B, Chem.*, vol. 173, pp. 338–345, Oct. 2012.

[43] E. R. F. Welch, Y.-Y. Lin, A. Madison, and R. B. Fair, "Picoliter DNA sequencing chemistry on an electrowetting-based digital microfluidic platform," *Biotechnol. J.*, vol. 6, no. 2, pp. 165–176, 2011.

[44] K. H. Kang, "How electrostatic fields change contact angle in electrowetting," *Langmuir*, vol. 18, no. 26, pp. 10318–10322, 2002.

[45] K. H. Kang, I. S. Kang, and C. M. Lee, "Wetting tension due to Coulombic interaction in charge-related wetting phenomena," *Langmuir*, vol. 19, no. 13, pp. 5407–5412, 2003.

Andrew C. Madison received the B.S. degrees in chemistry and biology, and the M.S. degree in physics from Appalachain State University in 2007 and 2009, respectively, and the Ph.D. degree in electrical and computer engineering from Duke University in 2015. His research interests include device physics, finite element modeling, microfabrication, fluid dynamics, and digital microfluidics. He received the Department of Defence Fellowship for Science, and Mathematics and Research for Transformation.

Matthew W. Royal received the Ph.D. degree in electrical engineering from Duke University, Durham, NC, USA, in 2012, and the B.S. degree in engineering science from Pennsylvania State University, State College, PA, USA, in 2006. He is currently with Holographix LLC, Hudson, MA.

Richard B. Fair (S'63–M'75–SM'75–F'90–LF'09) received the Ph.D. degree in electrical engineering from Duke University in 1969. He is currently a Lord-Chandran Professor of Engineering with Duke. He joined Bell Laboratories, where he was involved in semiconductor devices, integrated circuits, and semiconductor process technologies. In 1981, he joined MCNC as a Vice President, where he led the Center for Microelectronic Systems from 1981-1994. Concurrently, he held a joint appointment with Duke as a Professor of Electrical Engineering. In 1994, he returned to Duke. In 1999, his group produced the first electrowetting-on-dielectric chip, thus demonstrating digital microfluidics. The students involved spun out Advanced Liquid Logic, Inc. His current research areas include digital microfluidic devices, applications, and technology. He is a fellow of the Electrochemical Society. He is a recipient of the IEEE Third Millennium Medal in 2000, and the 2003 Solid-State Science and Technology Prize and Medal from the Electrochemical Society, which was presented in Paris, France. He was an Editor-in-Chief of the PROCEEDINGS OF THE IEEE. He has served as an Associate Editor of the IEEE TRANSACTIONS ON ELECTRON DEVICES.